

Automatic prostate cancer detection through DCE-MRI images: all you need is a good normalization

Guillaume Lemaître^{a,b,*}, Robert Martí^b, Fabrice Meriaudeau^{a,c}

^a*LE2I UMR6306, CNRS, Arts et Métiers, Univ. Bourgogne Franche-Comté, 12 rue de la Fonderie, 71200 Le Creusot, France*

^b*ViCOROB, Universitat de Girona, Campus Montilivi, Edifici P4, 17071 Girona, Spain*

^c*CISIR, Electrical & Electronic Engineering Department, Universiti Teknologi Petronas, 32610 Seri Iskandar, Perak, Malaysia*

Abstract

This template helps you to create a properly formatted L^AT_EX manuscript.

Keywords: DCE-MRI, prostate cancer, normalization, classification, quantification

1. Introduction

Prostate Cancer (PCa) is the second most frequently diagnosed men cancer, accounting for 899,000 cases leading to 258,100 deaths (Ferlay et al., 2010). As highlighted by the PI-RADS Steering Committee, the two main challenges
5 to be addressed are (Weinreb et al., 2016): (i) the improvement of detecting clinically significant PCa and (ii) an increase of the confidence in benign or dormant cases, avoiding unnecessary invasive medical exams. In this regard, multiparametric Magnetic Resonance Imaging (MRI) (mp-MRI) is frequently
10 used to build robust Computer-Aided Detection and Diagnosis (CAD) systems to detect, localize, and grade PCa. In general, CAD systems are based on mp-MRI which potentially combines several of the following modalities (Lemaître et al., 2015): T₂ Weighted (T₂-W)-MRI, Dynamic Contrast-Enhanced (DCE)-MRI, Apparent Diffusion Coefficient (ADC) maps, and Magnetic Resonance Spectroscopy Imaging (MRSI).

*Corresponding author.

Email address: g.lemaitre58@gmail.com (Guillaume Lemaître)

15 In DCE-MRI, a contrast media is injected intravenously and a set of images is acquired over time. Consequently, each voxel in an image corresponds to a dynamic signal which is related to both contrast agent concentration and the vascular properties of the tissue. Therefore, changes of the enhanced signal allows to discriminate healthy from PCa tissues. In fact, these properties are automat-
20 ically extracted using quantitative or semi-quantitative approaches (Lemaître et al., 2015).

Quantitative approaches uses pharmacokinetic modelling based on a bicompart-
ment model, namely Brix (Brix et al., 1991) and Tofts (Tofts et al., 1995) models. The parameters of the Brix model are inferred assuming a linear rela-
25 tionship between the media concentration and the MRI signal intensity. This assumption has shown, however, to lead to inaccurately estimate the pharmacokinetic parameters (Heilmann et al., 2006). In the contrary, Tofts model requires a conversion from MRI signal intensity to concentration, which become a non-linear relationship using specific equation of MRI sequences (e.g., FLASH
30 sequence). Tofts modelling suffers, however, from an higher complexity (Gliozzi et al., 2011). Indeed, the conversion using the non-linear approach requires to acquire a T_1 map which is not always possible during clinical examination. Additionally, the parameter calculation requires the Arterial Input Function (AIF) which is challenging to measure and can also lead to inaccurate estimation.

35 *Semi-quantitative* approaches are rather mathematical than pharmacokinetic modelling (Huisman et al., 2001; Gliozzi et al., 2011). These methods offer the advantages to not require any knowledge about the MRI sequence nor any conversion from signal intensity to concentration. However, the heuristic approach propose by Huisman et al. requires an estimate regarding the noise standard
40 deviation of the signal as well as manual tuning.

Nevertheless, all presented methods suffer from two major drawbacks: (i) inter-patient variability and (ii) loss of information. The inter-patient variability is mainly due to the acquisition process and consequently lead to generalization issue while applying machine learning algorithm. All previous methods extract
45 few discriminative parameters to describe the DCE-MRI signal which might

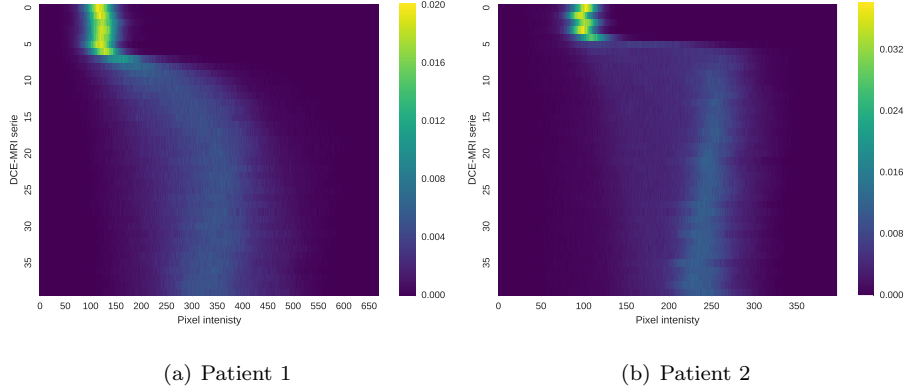


Figure 1: Illustration of the variations of the intensity PDF over time of two patients in a DCE-MRI.

lead to a loss of information.

In this work, we propose a fully automatic normalization method for DCE-MRI that reduce the inter-patient variability of the data. The benefit of our approach will be shown while using quantitative and semi-quantitative approaches. Additionally, we show that using the whole normalized DCE-MRI signal is preferable to quantitative and semi-quantitative methods, leading to the best classification performance.

The paper is organized as follows: Section 2.1 presents into details our normalization strategy for DCE-MRI data. Quantitative and semi-quantitative methods are summarized in Sect. 2.2 with insights about their implementations. Section 3 gives information about the dataset used and provided source code. Experiments and results to answer the previous stated challenges are reported in Sect. 4 while discussed in Sect. 5, followed by a concluding section.

2. Methods

2.1. Normalization of DCE-MRI images

In this work, we propose a method to normalize DCE-MRI prostate data, although it can be applied to any DCE-MRI sequences. The aim of the method is

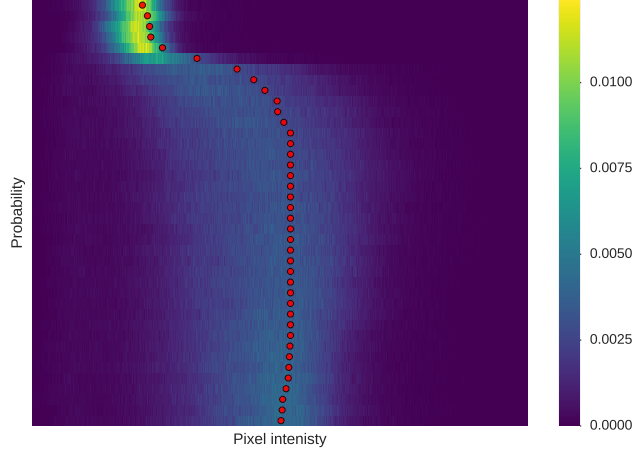


Figure 2: Illustration of the estimator found using the shortest-path through the graph.

to reduce the intra-patient variations, occurring during the acquisition process. In T_2 -W-MRI, these variations imply that the intensity Probability Density Function (PDF) of the prostate region is shifted as well as wider or narrower,
65 from a patient to another. Therefore, these variations can be corrected using a z -score approach, assuming that the data follow a specific distribution (Lemaitre et al., 2016).

In DCE-MRI, the inter-patient variations are more complex due to the over
70 time acquisition. These variations can be highlighted by observing the evolution of the intensity PDF of the DCE-MRI over time, as shown in the heatmap in Fig. 1. Therefore, these variations are: (i) an intensity offset of the PDF peak at pre-contrast, (ii) a time offset depending of the contrast agent arrival, and (iii) a change of scale related to the signal enhancement. Therefore, our normalization
75 method should attenuate all these variations and be performed globally across the different time sequence rather than for each independent sequence.

2.1.1. Graph-based offset correction for each DCE-MRI sequence

Before to standardize each sequence, the first step of the normalization is to cancel the intensity specific at each patient, occurring due to the media
80 injection. In DCE-MRI, the intensity PDF do not always follow either a Rician

or a Gaussian distribution over time. Therefore, the mean of these distributions cannot be used as a potential estimate for this offset. Additionally, this offset should be characterized by a smooth transition between series over time. Thus, this problem is solved using the graph-theory: considering the intensity PDF
85 over time as shown in Fig. 1, the offset is the boundary splitting the heatmap in two partitions such that it is as close as possible to the peak of the intensity PDF (see Fig. 2 for an illustration). Given the heatmap, a directed weighted graph $\mathcal{G} = (\mathcal{V}, \mathcal{E})$ is built by taking each bar of the heatmap as a node and connecting each pair of bars by an edge. The edge weight w_{ij} between two nodes i and
90 j corresponding to two pixels at position (x_i, y_i) and (x_j, y_j) , respectively, is defined as in Eq. (1):

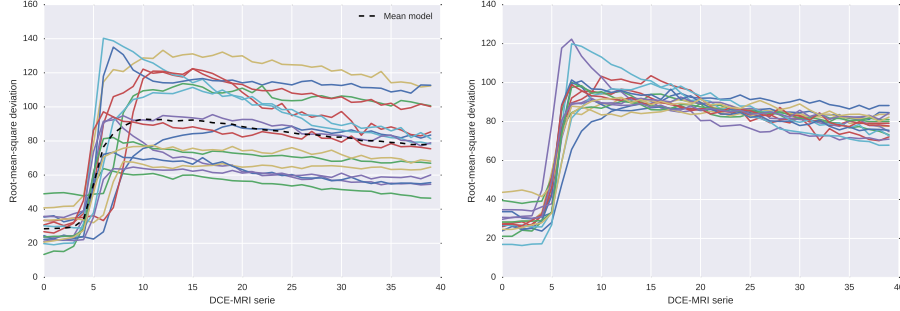
$$w_{ij} = \begin{cases} \alpha \exp(1 - \frac{H(i)}{\max(H)}) & \text{if } x_j = x_i + 1 \text{ and } y_j = y_i, \\ (1 - \alpha) \exp(1 - \frac{H(i)}{\max(H)}) & \text{if } x_j = x_i \text{ and } y_j = y_i + 1, \\ 0 & \text{otherwise,} \end{cases} \quad (1)$$

where H is the heatmap, α is a smoothing parameter controlling the partitioning.

Therefore, the offset is estimated by finding the shortest-path to cross the
95 graph using Dijkstra's algorithm. The entry and exiting nodes are set to be the bin with the maximum probability for the first DCE-MRI serie and the bin corresponding to the median value for the last DCE-MRI serie, respectively. To ensure a robust estimation of the offset, the process of finding the shortest-path is iteratively repeated by shifting the data and updating the heatmap as well
100 as the graph \mathcal{G} . The procedure is stopped once that the offset found do not change. In general, this process is not repeated more than 3 iterations. An example of the offset found using this approach is presented in Fig. 2. Finally, for each DCE-MRI serie, the intensities are shifted by this offset.

2.1.2. Time offset and data dispersion correction

105 The next variations to correct are the time offset and the data dispersion. By computing the Root-Mean-Square Deviation (RMSD) of the intensities for each



(a) RMSD computed for each patient of our dataset. (b) RMSD after alignment using the curve parametric model.

Figure 3: Illustration of the correction of the time offset and the data dispersion.

DCE-MRI serie, one can observed these two variations as shown in Fig. 3(a). Therefore, to correct these variations, we propose to register each patient RMSD to a mean model which corresponds to the mean of all patients RMSD. The
110 parametric model to perform the registration is formulated as in Eq. (2):

$$T(\alpha, \tau, f(t)) = \alpha f(t - \tau), \quad (2)$$

where α and τ are the two parameters handling the time offset and global scale, respectively, $f(\cdot)$ is the RMSD function.

Therefore the registration problem is equivalent to:

$$\arg \min_{\alpha, \tau} = \sum_{t=0}^N [T(\alpha, \tau, f(t)) - \mu(t)]^2, \quad (3)$$

where $\mu(\cdot)$ is the mean model, N is the number of DCE-MRI serie.

115 Illustration of the correction applied to each RMSD patient is shown in Fig. 3(b). Once all these parameters have been inferred, the data can be shifted as well as scaled.

2.2. Quantification of DCE-MRI

2.2.1. Brix and Hoffmann models

120 In the Brix model (Brix et al., 1991), the MRI signal intensity is assumed to be proportional to the media concentration. Therefore, the model is expressed as in Eq. (4):

$$s_n(t) = 1 + A \left[\frac{\exp(k_{el}t') - 1}{k_{ep}(k_{ep} - k_{el})} \exp(-k_{el}t) - \frac{\exp(k_{ep}t') - 1}{k_{el}(k_{ep} - k_{el})} \exp(-k_{ep}t) \right], \quad (4)$$

with

$$s_n(t) = \frac{s(t)}{S_0}, \quad (5)$$

where $s(t)$ and S_0 are the MRI signal intensity at time t and the average pre-contrast MRI signal intensity, respectively; A , k_{el} , and k_{ep} are a constant proportional to the transfer constant, the diffusion rate constant, and the rate constant, respectively. Additionally, during the injection time $0 \leq t \leq \tau$, $t' = t$ and afterwards while $t > \tau$, $t' = \tau$.

Following this model, Hoffmann et al. propose the following similar model
130 as expressed in Eq. (6):

$$s_n(t) = 1 + \frac{A}{\tau} \left[\frac{k_{ep}(\exp(k_{el}t') - 1)}{k_{el}(k_{ep} - k_{el})} \exp(-k_{el}t) - \frac{\exp(k_{ep}t') - 1}{(k_{ep} - k_{el})} \exp(-k_{ep}t) \right]. \quad (6)$$

The parameters are estimated by fitting the model using non-linear least-squares optimization solved with Levenberg-Marcquardt.

2.2.2. Tofts model

The extended Tofts model is formulated as in Eq. (7):

$$C_t(t) = K_{trans}C_p(t) * \exp(-k_{ep}t) + v_pC_p(t), \quad (7)$$

135 where $*$ is the convolution operator; $C_t(t)$ and $C_p(t)$ is the concentration of contrast agent in the tissue and in the plasma, respectively; K_{trans} , k_{ep} , and v_p

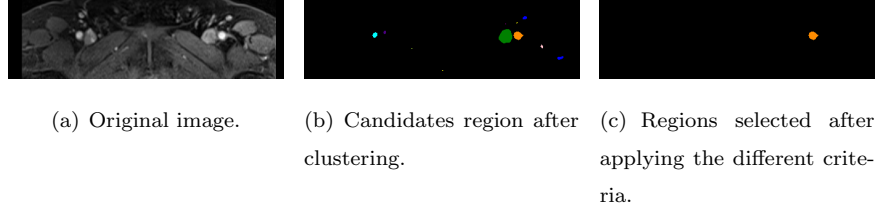


Figure 4: Illustration of the segmentation of the area used to determine the AIF.

are the volume transfer constant, the diffusion rate constant, and the plasma volume fraction, respectively.

Therefore, Tofts model requires to: (i) detect candidate voxels from the femoral or iliac arteries and estimate a patient-based AIF signal, (ii) convert the MRI signal intensity (i.e., AIF and dynamic signal) to a concentration, and (iii) in the case of a population-based AIF, estimate an AIF signal.

Segmentation of artery voxels and patient-based AIF estimation

The AIF signal from DCE-MRI can be manually estimated by selecting the most-enhanced voxels from the femoral or iliac arteries (Meng et al., 2010). Few methods have been proposed to address the automated extraction of AIF signal. Chen et al. filter successively the possible candidates (Chen et al., 2008): (i) dynamic signals with small peak are rejecting by thresholding, (ii) voxels with a small wash-in are rejected by thresholding, (iii) a blob detector is used and large enough regions are kept, and (iv) circular and cylindricity are used to reject the last false positive. Zhu et al. propose an iterative method selecting voxels which best fit a gamma variate function (Zhu et al., 2011). However, it requires to compute first and second derivatives as well as maximum curvature points. Shanbhag et al. propose a 4-steps algorithm (Shanbhag et al., 2012; Fennessy et al., 2015): (i) remove slices with artefacts and find the best slices based on intrinsic anatomic landmarks and enhancement characteristics, (ii) find the voxel candidates using the maximum enhanced voxels and a multi-label maximum entropy based thresholding algorithm, (iii) excluding region next to

160 the endorectal coil, and (iv) selecting the best 5 candidates which meet enhancement characteristics and that are correlated.

All the above methods are rather complex and thus we propose a method which is based on the following simple assumptions: (i) all possible AIF signal candidates should have a similar shape, (ii) an high enhancement, 165 and (iii) the arteries should be almost round and within a size range. Therefore, each slice is clustered into regions using K-means clustering with $k = 6$. The cluster with the highest enhancement—i.e. corresponding to the 90th percentile of the maximum of each dynamic signal—contain the arteries and is selected. Finally, regions with an eccentricity smaller than 170 0.5 and an area in the range of $[100, 400]$ voxels are kept. Additionally, to remove voxels contaminated by partial volume effect, only the 10% most enhanced voxels of the possible candidates are kept as proposed by (Schabel and Parker, 2008) and the average signal is computed. A summary of the different segmentation steps is presented in Fig. 4.

Conversion of MRI signal intensity to concentration To estimate the free parameters of the Tofts model (see Eq. (7)), the concentration $C_t(t)$ and $C_p(t)$ need to be computed from the MRI signal intensity and the AIF signal, respectively. This conversion is based on the equation of the FLASH sequence—see Appendix A for details—and is formulated as in Eq. (8):

$$c(t) = \frac{1}{TR \cdot r_1} \ln \left(\frac{1 - \cos \alpha \cdot S^* \frac{s(t)}{S_0}}{1 - S^* \frac{s(t)}{S_0}} \right) - \frac{R_{10}}{r_1}, \quad (8)$$

with,

$$S^* = \frac{1 - \exp(-TR \cdot R_{10})}{1 - \cos \alpha \cdot \exp(-TR \cdot R_{10})}, \quad (9)$$

175 where $s(t)$ is the MRI signal, S_0 is the MRI signal prior to the injection of the contrast media, α is the flip angle, TR is the Repetition Time (TR), R_{10} is the pre-contrast tissue relaxation time also equal to $\frac{1}{T_{10}}$, r_1 is the relaxivity coefficient of the contrast agent.

T_{10} can be estimated from the acquisition of a T_1 map. However, this 180 modality was not part of the clinical trial in this research and the value of

T_{10} was fixed to 1600 ms for both blood and prostate as stated in the literature (Fennessy et al., 2015; De Bazelaire et al., 2004; Carr and Carroll, 2011).

Estimation of population-based AIF While estimating the pharmacokinetic parameters from Tofts model, the AIF concentration $C_p(t)$ can be computed either from the patient or a population. We presented in the two previous sections the algorithms which allows to estimate the patient-based AIF concentration. To compare with the previous approach, we also computed a population-based AIF which will be also later used to compare the performance of both approaches. In that regard, the population-based AIF was estimated as in (Meng et al., 2010) by fitting the average patient-based AIFs to the model of Parker et al. (2006) which is formulated as in Eq. (10):

$$C_p(t) = \sum_{n=1}^2 \frac{A_n}{\sigma_n \sqrt{2\pi}} \exp\left(\frac{-(t - T_n)^2}{2\sigma_n^2}\right) + \frac{\alpha \exp(-\beta t)}{1 + \exp -s(t - \tau)}, \quad (10)$$

where A_n , T_n , and σ_n are the scaling constants, centers, and widths of the n^{th} Gaussian, α and β are the amplitude and decay constant of the exponential; and s and τ are the width and center of the sigmoid function, respectively.

The parameters are estimated by fitting the model using non-linear least-squares optimization solved with Levenberg-Marcquardt.

2.2.3. PUN model

Glozzi et al. show that Phenomenological Universalities (PUN) approach can be used for DCE-MRI analysis (Glozzi et al., 2011). The model has been successfully used in a CAD system proposed by Giannini et al. (2015). This model can be expressed as in Eq. (11):

$$s_n(t) = \exp\left[rt + \frac{1}{\beta}(a_0 - r)(\exp(\beta t) - 1)\right], \quad (11)$$

195 with

$$s_n(t) = \frac{s(t) - S_0}{S_0}, \quad (12)$$

where $s(t)$ and S_0 are the MRI signal intensity at time t and the average pre-contrast MRI signal intensity, respectively; r , a_0 , and β are the free parameters of the model.

The parameters are estimated by fitting the model using non-linear least-squares optimization solved with Levenberg-Marcquardt.
200

2.2.4. Semi-quantitative analysis

The semi-quantitative analysis of the DCE-MRI is equivalent to extract curve characteristics directly from the signal without a strict theoretical pharmacokinetic meaning. In this work, we use the model presented by Huisman et al. (2001) which formulate the MRI signal as in Eq. (13):
205

$$s(t) = \begin{cases} S_0 & 0 \leq t \leq t_0 \\ S_M - (S_M - S_0) \exp\left(\frac{-(t-t_0)}{\tau}\right) & t_0 < t \leq t_0 + 2\tau \\ S_M - (S_M - S_0) \exp\left(\frac{-(t-t_0)}{\tau}\right) + w(t - t_0 + 2\tau) & t > t_0 + 2\tau \end{cases} \quad (13)$$

where $s(t)$ is the MRI signal intensity, S_0 is the pre-contrast signal intensity, t_0 is the time corresponding to the start of enhancement, S_M and τ is the maximum of the signal and the exponential time constant, and w is the slope of the linear part.

Huisman et al. argue that curve fitting via least-squares minimization using
210 Nelder-Mead algorithm leads to inaccurate estimation of the free parameters: mainly the issue come from an incorrect estimation of the start of enhancement t_0 leading to incorrect estimation of the other parameters. Therefore, they propose to: (i) estimate robustly t_0 , (ii) estimate S_0 by averaging the samples
215 between 0 and t_0 (ii) estimate w depending if the slope is significant or not, (iii)

estimate S_M which should be the point at the intersection of the most probable slope line and the plateau.

Instead of these successive estimations, we propose a unified optimization in which t_0 is fixed since that this is a key parameter. Therefore, t_0 is robustly
220 estimated from the AIF signal since that this is the most enhanced signal in which the start of enhancement is easily identifiable. The AIF signal is computed as in Section 2.2.2. t_0 is estimated by finding the maximum in the beginning of the first derivative of the MRI signal. Then, the function in Eq.(13) is fitted using non-linear least squares with Trust Region Reflective algorithm.
225 Furthermore, the parameters τ and S_M are bounded during the optimization to ensure robust estimations.

From Eq.(13), the following features are extracted: (i) the wash-in corresponding to the slope between t_0 and $t_0 + 2\tau$, (ii) the wash-out corresponding to the parameter w , (iii) the area under the curve between t_0 and the end of the
230 signal, (iv) the exponential time constant τ , and (v) the relative enhancement $S_M - S_0$.

3. Materials

3.1. Data

The multi-parametric MRI data are acquired from a cohort of patients with
235 higher-than-normal level of Prostate-Specific Antigen (PSA). The acquisition is performed using a 3T whole body MRI scanner (Siemens Magnetom Trio TIM, Erlangen, Germany) using sequences to obtain T₂-W-MRI, DCE-MRI and Diffusion Weighted (DW)-MRI. Aside of the MRI examination, these patients also have underwent a guided-biopsy. The dataset is composed of a total of
240 20 patients of which 18 patients have biopsy proven PCa and 2 patients are “healthy” with negative biopsies. Therefore, 13 patients have a PCa in the Peripheral Zone (PZ), 3 patients have PCa in the Central Gland (CG), 2 patients have invasive PCa in both PZ and CG and finally 2 patients are considered as “healthy”. An experienced radiologist has segmented the prostate organ — on

245 T₂-W-MRI and DCE-MRI — as well as the prostate zones (i.e., PZ and CG) and PCa on the T₂-W-MRI.

A 3 mm slice fat-suppressed T₂-W fast spin-echo sequence (TR/Echo Time (TE)/Echo Train Length (ETL): 3400 ms/85 ms/13) is used to acquire images in sagittal and oblique coronal planes, the latter planes being orientated perpendicular or parallel to the prostate PZ rectal wall axis. Three-dimensional T₂-W
250 fast spin-echo (TR/TE/ETL: 3600 ms/143 ms/109, slice thickness: 1.25 mm) images are then acquired in an oblique axial plane. The nominal matrix and Field Of View (FOV) of the 3D T₂-W fast spin-echo images are 320×256 and 280×240 mm², respectively, thereby affording sub-millimetric pixel resolution
255 within the imaging plane.

DCE-MRI are performed using a fat suppressed 3D T₁ VIBE sequence (TR/TE/Flip angle: 3.25 ms/1.12 ms/10°; Matrix: 256×192 ; FOV: 280×210 (with 75% rectangular FOV); slab of 16 partitions of 3.5 mm thickness; temporal resolution: 6 s/slab over approximately 5 min). A power injector (Medrad,
260 Indianola, USA) is used to provide a bolus injection of Gd-DTPA (Dotarem, Guerbet, Roissy, France) at a dose of 0.2 ml Gd-DTPA/kg of body weight.

These DCE-MRI sequences are resampled using the spatial information of the T₂-W-MRI and missing data are interpolated using linear interpolation. The volumes of the DCE-MRI dynamic are rigidly registered, to remove any
265 patient motion during the acquisition. Furthermore, a non-rigid registration is performed between the T₂-W-MRI and DCE-MRI in order to propagate the prostate zones and PCa ground-truths. The resampling is implemented in C++ using the Insight Segmentation and Registration Toolkit (Ibanez et al., 2005).

3.2. Implementation

270 The implementation of the registration (C++), normalization (Python), and classification pipeline (Python) are publicly available on GitHub¹. The data

¹<https://github.com/I2Cvb/lemaitre-2016-nov/tree/master>

used for this work are also publicly available².

4. Experiments and results

4.1. Classification of individual parameter for each model

275 The first experiment consists in comparing the classification performance using each individual parameter for the different models, to assess the potential benefit of the normalization method. Therefore, each feature is individually classified using a Gaussian Naive Bayes (NB) classifier in a Leave-One-Patient-Out Cross-Validation (LOPO CV) fashion. NB is used due to its simplicity
280 and it enables to check the fitted parameters for interpretation. The results are summarized in Table 1. It can be noted that in the majority of the cases, normalizing the data improve the classification performance in terms of Area Under the Curve (AUC). Only the PUN model does not follow this tendency which might due to the fact that the function do not fit the data as good as the
285 other model - WE WILL NEED SOME RMSE FOR EACH FITTING IF WE SAY SO..

It could be interesting to check the value of the mean and std of the NB. We could compute a ratio which refer to the class separability.

4.2. Classification by combining the parameters for each model

290 Usually, the parameters are combined to form a multi-dimensional prior to classify the data. Therefore, for each model, all parameters are combined and classified using a Random Forest (RF) classifier in a LOPO CV fashion. The use of RF is motivated since that it leads to the best performance in the state-of-the-art methods (Litjens et al., 2014). The results are summarized by making
295 Receiver Operating Characteristic (ROC) analysis and computing the AUC, as reported in Fig. 5. It can be noted that in all the cases the normalization of the data improve the classification performance.

²<http://kaggle.com>

Table 1: AUC for each individual pharmacokinetic parameter using a NB classifier.

Features	Un-normalized data	Normalized data
Brix model		
A	0.62	0.67
k_{el}	0.52	0.61
k_{ep}	0.52	0.58
Hoffmann model		
A	0.50	0.56
k_{el}	0.53	0.64
k_{ep}	0.50	0.66
Tofts model with population AIF		
K_{trans}	0.62	0.65
v_e	0.50	0.52
v_p	0.63	0.53
Tofts model with patient AIF		
K_{trans}	0.66	0.65
v_e	0.50	0.52
v_p	0.37	0.65
PUN model		
a_0	0.53	0.51
r	0.59	0.55
β	0.56	0.44
Semi-quantitative analysis		
wash-in	0.64	0.51
wash-out	0.50	0.66
IAUC	0.61	0.64
τ	0.57	0.61
$S_M - S_0$	0.63	0.64

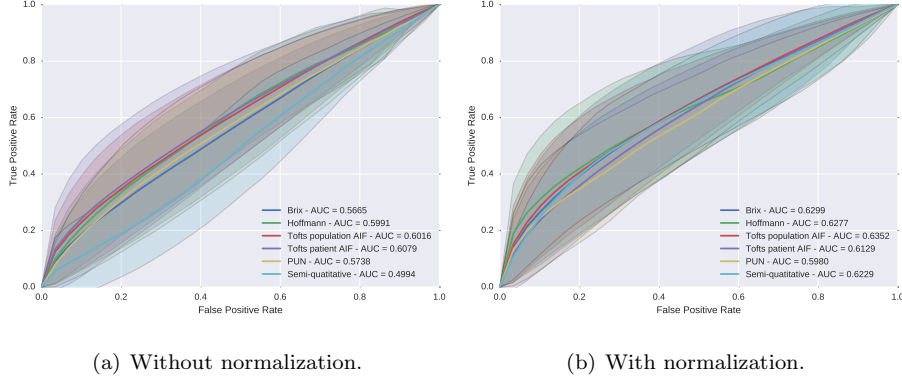


Figure 5: ROC analysis using a RF classifier with and without normalization DCE-MRI data for different pharmacokinetic models.

4.3. Classification of the entire enhanced DCE-MRI signal

The quantification methods are extracting a minimal set of parameters which should characterized the enhancement DCE-MRI curves. However, this extraction could discard some information of the signal. This experiment attends to use the whole DCE-MRI signal to perform the classification. Therefore, the enhanced signal is classified using a RF classifier in a LOPO CV fashion. The ROC analysis and AUC are reported in Fig. 6. It can be note that the worst performance are achieved while data without normalization. However, normalizing the data, this classification strategy lead the best classification performance, outperforming any quantification method, showing the importance of our normalization algorithm.

5. Discussions

- Discuss about the T1 parameters in Tofts and say that we can do better probably.
- Compare the two approach for the AIF.
- Make a discussion about the detailed interpretation of individual feature classification. There is something to discuss about the semi-quantitative

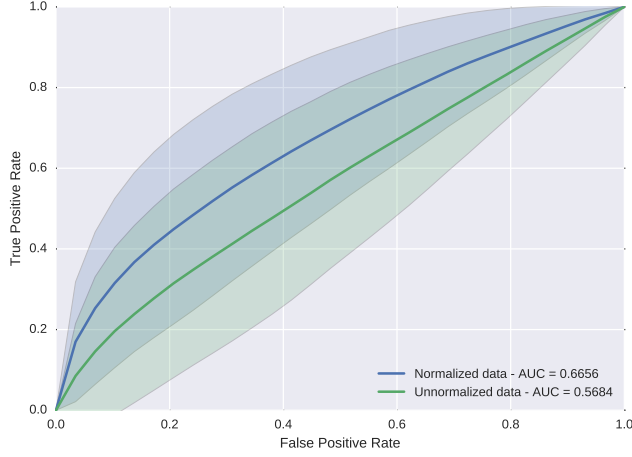


Figure 6: ROC analysis using the entire DCE-MRI signal with and without normalization in conjunction with a RF classifier.

315 from wash-in to wash-out reversed performance. Something also about the PUN model.

- Explain the drawbacks of the whole signal classification (time).

6. Conclusions and future works

In this work, we presented a new method for normalizing/standardizing DCE-MRI data. Through different experiments, we show the benefit of such 320 normalization. Furthermore, we show that using the whole DCE-MRI signal instead extracting parameters lead to the best classification performance.

As avenues for future research, this normalization has to be part of a mp-MRI CAD system, mixing T₂-W-MRI, DCE-MRI, DW-MRI, and MRSI.

325 Appendix A. Conversion from FLASH signal to media concentration

In this appendix, we show the demonstration used to extract the agent concentration from the MRI signal.

The signal equation in FLASH sequence (Haase et al., 1986) is defined as:

$$s(t) = S_{eq} \sin \alpha \cdot \frac{1 - \exp(-TR(R_{10} + r_1 c(t)))}{1 - \cos \alpha \cdot \exp(-TR(R_{10} + r_1 c(t)))}, \quad (\text{A.1})$$

where $s(t)$ is the MRI signal, S_{eq} is the maximum signal amplitude of the spoiled
 330 gradient at the TE which is proportional to the Proton Density (PD), α is the flip
 angle, TR is the Repetition Time (TR), R_{10} is the pre-contrast tissue relaxation
 time also equal to $\frac{1}{T_{10}}$, r_1 is the relaxitivity coefficient of the contrast agent, and
 $c(t)$ is the media concentration.

Therefore, the pre-contrast signal prior to bolus injection of the media is
 335 defined as:

$$S_0 = S_{eq} \sin \alpha \cdot \frac{1 - \exp(-TR \cdot R_{10})}{1 - \cos \alpha \cdot \exp(-TR \cdot R_{10})}. \quad (\text{A.2})$$

To simplify the demonstration, let us define:

$$A = \exp(-TR \cdot R_{10}), \quad (\text{A.3})$$

$$B = \exp(-TR \cdot r_1 c(t)). \quad (\text{A.4})$$

Let us define:

$$S^* = \frac{S_0}{S_{eq} \sin \alpha}, \quad (\text{A.5})$$

$$= \frac{1 - A}{1 - A \cos \alpha}. \quad (\text{A.6})$$

Thus,

$$S^* \frac{s(t)}{S_0} = \frac{S_0}{S_{eq} \sin \alpha} \frac{s(t)}{S_0}, \quad (\text{A.7})$$

$$= \frac{1 - AB}{1 - AB \cos \alpha}. \quad (\text{A.8})$$

Now, let us define:

$$\frac{1 - \cos \alpha \cdot S^* \frac{s(t)}{S_0}}{1 - S^* \frac{s(t)}{S_0}} = \frac{1 - \cos \alpha \left(\frac{1-AB}{1-AB \cos \alpha} \right)}{1 - \frac{1-AB}{1-AB \cos \alpha}}, \quad (\text{A.9})$$

$$= \frac{1 - AB \cos \alpha - \cos \alpha (1 - AB)}{1 - AB \cos \alpha - (1 - AB)}, \quad (\text{A.10})$$

$$= \frac{1 - AB \cos \alpha - \cos \alpha + AB \cos \alpha}{1 - AB \cos \alpha - 1 + AB}, \quad (\text{A.11})$$

$$= \frac{1 - \cos \alpha}{AB(1 - \cos \alpha)}, \quad (\text{A.12})$$

$$= \frac{1}{AB}. \quad (\text{A.13})$$

340 Thus,

$$-TR \cdot R_{10} - TR \cdot r_1 c(t) = \ln \left(\frac{1 - \cos \alpha \cdot S^* \frac{s(t)}{S_0}}{1 - S^* \frac{s(t)}{S_0}} \right). \quad (\text{A.14})$$

Therefore,

$$c(t) = \frac{1}{TR \cdot r_1} \ln \left(\frac{1 - \cos \alpha \cdot S^* \frac{s(t)}{S_0}}{1 - S^* \frac{s(t)}{S_0}} \right) - \frac{R_{10}}{r_1}. \quad (\text{A.15})$$

References

- Brix, G., Semmler, W., Port, R., Schad, L.R., Layer, G., Lorenz, W.J., 1991. Pharmacokinetic parameters in cns gd-dtpa enhanced mr imaging. Journal of computer assisted tomography 15, 621–628.
- 345 Carr, J.C., Carroll, T.J., 2011. Magnetic resonance angiography: principles and applications. Springer Science & Business Media.
- Chen, J., Yao, J., Thomasson, D., 2008. Automatic determination of arterial input function for dynamic contrast enhanced mri in tumor assessment, in: International Conference on Medical Image Computing and Computer-Assisted Intervention, Springer. pp. 594–601. doi:10.1007/978-3-540-85988-8_71.
- 350 De Bazelaire, C.M., Duhamel, G.D., Rofsky, N.M., Alsop, D.C., 2004. Mr imaging relaxation times of abdominal and pelvic tissues measured in vivo at

- 3.0 t: preliminary results 1. *Radiology* 230, 652–659. doi:10.1148/radiol.2303021331.
- 355 Fennessy, F.M., Fedorov, A., Penzkofer, T., Kim, K.W., Hirsch, M.S., Vangel, M.G., Masry, P., Flood, T.A., Chang, M.C., Tempany, C.M., et al., 2015. Quantitative pharmacokinetic analysis of prostate cancer dce-mri at 3t: comparison of two arterial input functions on cancer detection with digitized whole mount histopathological validation. *Magnetic resonance imaging* 33, 886–894. doi:10.1016/j.mri.2015.02.008.
- 360 Ferlay, J., Shin, H.R., Bray, F., Forman, D., Mathers, C., Parkin, D.M., 2010. Estimates of worldwide burden of cancer in 2008: Globocan 2008. *International journal of cancer* 127, 2893–2917. doi:10.1002/ijc.25516.
- 365 Giannini, V., Mazzetti, S., Vignati, A., Russo, F., Bollito, E., Porpiglia, F., Stasi, M., Regge, D., 2015. A fully automatic computer aided diagnosis system for peripheral zone prostate cancer detection using multi-parametric magnetic resonance imaging. *Computerized Medical Imaging and Graphics* 46, 219–226. doi:10.1016/j.compmedimag.2015.09.001.
- 370 Gliozzi, A., Mazzetti, S., Delsanto, P.P., Regge, D., Stasi, M., 2011. Phenomenological universalities: a novel tool for the analysis of dynamic contrast enhancement in magnetic resonance imaging. *Physics in medicine and biology* 56, 573.
- 375 Haase, A., Frahm, J., Matthaei, D., Hanicke, W., Merboldt, K.D., 1986. Flash imaging. rapid nmr imaging using low flip-angle pulses. *Journal of Magnetic Resonance (1969)* 67, 258–266. doi:10.1016/0022-2364(86)90433-6.
- 380 Heilmann, M., Kiessling, F., Enderlin, M., Schad, L.R., 2006. Determination of pharmacokinetic parameters in dce mri: consequence of nonlinearity between contrast agent concentration and signal intensity. *Investigative radiology* 41, 536–543. doi:10.1097/01.rli.0000209607.99200.53.

- Hoffmann, U., Brix, G., Knopp, M.V., Heß, T., Lorenz, W.J., 1995. Pharmacokinetic mapping of the breast: a new method for dynamic mr mammography. *Magnetic resonance in medicine* 33, 506–514. doi:10.1002/mrm.1910330408.
- 385 Huisman, H.J., Engelbrecht, M.R., Barentsz, J.O., 2001. Accurate estimation of pharmacokinetic contrast-enhanced dynamic mri parameters of the prostate. *Journal of Magnetic Resonance Imaging* 13, 607–614. doi:10.1002/jmri.1085.
- Ibanez, L., Schroeder, W., Ng, L., Cates, J., 2005. The itk software guide .
- 390 Lemaitre, G., Dastjerdi, M.R., Massich, J., Vilanova, J.C., Walker, P.M., Freixenet, J., Meyer-Baese, A., Mériaudeau, F., Marti, R., 2016. Normalization of t2w-mri prostate images using rician a priori, in: *SPIE Medical Imaging, International Society for Optics and Photonics*. pp. 978529–978529. doi:10.1117/12.2216072.
- 395 Lemaître, G., Martí, R., Freixenet, J., Vilanova, J.C., Walker, P.M., Meriaudeau, F., 2015. Computer-aided detection and diagnosis for prostate cancer based on mono and multi-parametric mri: A review. *Computers in biology and medicine* 60, 8–31. doi:10.1016/j.combiomed.2015.02.009.
- 400 Litjens, G., Debats, O., Barentsz, J., Karssemeijer, N., Huisman, H., 2014. Computer-aided detection of prostate cancer in mri. *IEEE transactions on medical imaging* 33, 1083–1092. doi:10.1109/TMI.2014.2303821.
- Meng, R., Chang, S.D., Jones, E.C., Goldenberg, S.L., Kozlowski, P., 2010. Comparison between population average and experimentally measured arterial input function in predicting biopsy results in prostate cancer. *Academic radiology* 17, 520–525. doi:10.1016/j.acra.2009.11.006.
- 405 Parker, G.J., Roberts, C., Macdonald, A., Buonaccorsi, G.A., Cheung, S., Buckley, D.L., Jackson, A., Watson, Y., Davies, K., Jayson, G.C., 2006.

- Experimentally-derived functional form for a population-averaged high-temporal-resolution arterial input function for dynamic contrast-enhanced mri. *Magnetic resonance in medicine* 56, 993–1000. doi:10.1002/mrm.21066.
- Schabel, M.C., Parker, D.L., 2008. Uncertainty and bias in contrast concentration measurements using spoiled gradient echo pulse sequences. *Physics in medicine and biology* 53, 2345. doi:10.1088/0031-9155/53/9/010.
- Shanbhag, D., Gupta, S.N., Rajamani, K., Zhu, Y., Mullick, R., 2012. A generalized methodology for detection of vascular input function with dynamic contrast enhanced perfusion data, in: *ISMRM*, p. 10.
- Tofts, P.S., Berkowitz, B., Schnall, M.D., 1995. Quantitative analysis of dynamic gd-dtpa enhancement in breast tumors using a permeability model. *Magnetic Resonance in Medicine* 33, 564–568. doi:10.1002/mrm.1910330416.
- Weinreb, J.C., Barentsz, J.O., Choyke, P.L., Cornud, F., Haider, M.A., Macura, K.J., Margolis, D., Schnall, M.D., Shtern, F., Tempany, C.M., et al., 2016. PIRADS prostate imaging-reporting and data system: 2015, version 2. *European urology* 69, 16–40.
- Zhu, Y., Chang, M.C., Gupta, S., 2011. Automated determination of arterial input function for dce-mri of the prostate, in: *SPIE Medical Imaging*, International Society for Optics and Photonics. pp. 79630W–79630W. doi:10.1117/12.878213.